Rare Metal Materials and Engineering
Volume 52, Issue 11, November 2023
Available online at www.rmme.ac.cn

Science Press

Cite this article as: He Ronghui, Wang Han, Zhang Ze, et al. Microstructure Characteristics, Mechanical Properties, and In-Vitro Corrosion Behavior of As-Extruded Mg-2Zn-0.5Gd-1Y-0.5Mn Mg Alloys[J]. Rare Metal Materials and Engineering, 2023, 52(11): 3697-3706. DOI: 10.12442/j.issn.1002-185X.20230192.

ARTICLE

Microstructure Characteristics, Mechanical Properties, and In-Vitro Corrosion Behavior of As-Extruded Mg-2Zn-0.5Gd-1Y-0.5Mn Mg Alloys

He Ronghui[1], Wang Han[2], Zhang Ze[3,4], Li Jingyuan[2], Wen Liangyuan[3,4]

[1] Nuclear Power Institute of China, China National Nuclear Corporation, Chengdu 610213, China; [2] School of Materials Science and Engineering, University of Science and Technology Beijing, Beijing 100083, China; [3] Department of Orthopedics, Beijing Hospital, Beijing 100730, China; [4] National Center of Gerontology, Chinese Academy of Medical Sciences, Beijing 100730, China

Abstract: In order to ameliorate the microstructure characteristics and degradation behavior of the medical Mg alloys, the extrusion process was conducted to change the grain size characteristics and the distribution law of secondary precipitates/intermetallic compounds, and the microstructure characteristics and degradation behavior of as-extruded Mg-2Zn-0.5Gd-1Y-0.5Mn Mg alloy were analyzed. Results show that different hot-extrusion deformation methods do not change the types of the secondary phases in Mg-2Zn-0.5Gd-1Y-0.5Mn Mg alloy, but change their distribution and morphology. The main components of Mg-2Zn-0.5Gd-1Y-0.5Mn Mg alloy are α-Mg and W-$Mg_3Y_2Zn_3$ phases. The electrochemical tests demonstrate that the corrosion current densities are 2.498, 3.656, and 1.012 $\mu A \cdot cm^{-2}$ for as-cast, extruded/370 °C, and extruded/390 °C Mg alloys, respectively. The precipitates/intermetallic compounds of strip shape are distributed in the matrix of as-cast Mg alloy, which can act as the micro-cathode, thus forming the galvanic-corrosion sites and accelerating the corrosion rates. Partial coarse precipitates cannot completely dissolve into the α-Mg matrix due to the low actual temperature of the Mg alloy during extrusion at 370 °C. With the disordered distribution and the increasing precipitates, the area proportion of micro-cathode is increased, which accelerates the corrosion rate. However, for the Mg alloy during extrusion at 390 °C, the extrusion speed is fast, the dissipation behavior is slow, and the friction between ingot and extruder is intense, indicating the occurrence of sufficient dynamic recrystallization, which reduces the number/area of micro-cathode and improves the corrosion resistance.

Key words: extrusion temperature; microstructure; precipitate phase; corrosion behavior; degradable Mg alloys

Recently, magnesium alloys, acting as the degradable medical materials, show great application potential and development prospect due to their good biocompatibility, unique degradability, and suitable modulus for human bone[1–7]. However, the extremely rapid corrosion rate of Mg alloys restricts their practical application, and the resultant hydrogen release can easily cause premature failure of implanted materials[8–14]. Therefore, the improvement in corrosion resistance of Mg alloys has been widely researched. Currently, rare earth alloying method is an important method to improve the corrosion resistance of medical Mg-based alloys. The rare earth elements with appropriate electronic value, crystal structure, and solid solubility are preferred in the practical application.

As a typical heavy rare earth element, Gd is a surface-active element with the densely close-packed hexagonal (hcp) crystal structure (a=0.362 nm, c=0.576 nm), which can promote the non-uniform nucleation and is beneficial to grain refinement[15]. In addition, the solid solubility of Gd element in hcp Mg alloy is high (4.53at% at 548 °C) and it is decreased rapidly with decreasing the heat treatment temperature[16–18]. Thus, an ideal precipitation strengthening system can be achieved. The solid solubility of Y element in Mg alloys is about 12.47wt%, and it is significantly decreased with decreasing the temperature. As a result, the solid strengthening

Received date: April 08, 2023
Foundation item: National Key Research and Development Plan of China (2022YFC3601905, 2022YFC3601900); National High Level Hospital Clinical Research Funding (BJ-2023-085)
Corresponding author: Wen Liangyuan, Ph. D., Professor, Department of Orthopedics, Beijing Hospital, Beijing 100730, P. R. China, E-mail: wenliangyuan1964@126.com

and grain refinement effects are obvious[19–22]. Yin et al[23] analyzed the corrosion behavior of as-cast $MgZn_{1.2}Gd_xZr_{0.18}$ alloy in 3.5wt% NaCl solution and found that with increasing the Gd content from 0at% to 2.0at%, the $MgZn_2$, W, *X*, and other secondary precipitates are continuously formed, the grains are refined, and the internal texture strength of the alloys is decreased gradually. Wang et al[24] investigated the stress-corrosion behavior of as-cast Mg-7Gd-5Y-1Nd-0.5Zr alloy in 3.5wt% NaCl electrolyte and revealed that a large number of Mg_5Gd precipitates exist in the matrix, which can act as the cathode phase to accelerate the corrosion, resulting in a large amount of hydrogen and leading to corrosion cracking behavior. Dai et al[25] discussed the effect of Y addition on the microstructure, mechanical properties, and corrosion behavior of as-cast Mg-Gd-Y-Zr-Ca-Zr Mg alloys. It is demonstrated that all alloys are composed of α-Mg matrix, eutectic phase, and lamellar stacking faults (SFs) which are located at the outer edge of the α-Mg grains. The higher Y content leads to the nano-hardness enhancement of the α-Mg matrix and more uniform hardness distribution. Additionally, the as-cast alloy with 3wt% Y content presents the most uniform corrosion morphology and has the slowest corrosion rate among the Y-modified Mg alloys. This is because the eutectic phase and SF/long period stacking orderly structure have better corrosion resistance than the α-Mg matrix does. Besides, SFs at the outer edge of α-Mg grains may play a significant role in the balance process of potential difference of different precipitates at α-Mg grain boundaries, which suppresses the interior corrosion of the alloys.

In order to further improve the corrosion resistance of Mg alloy, some deformation processes are used to optimize the microstructure characteristics, especially the extrusion process[26–32]. The extrusion process can refine the coarse dendrite microstructures, eliminate the micro-cracks inside the cast blank, and modify the distribution of precipitations, thereby improving the corrosion resistance of Mg alloys[33–36]. Hu et al[37] investigated the effect of Gd, Sn, and Cu elements on the corrosion behavior of as-extruded Mg-8Li-3Al (LA83) alloys through Kelvin probe force microscope (KPM), mass loss analysis, hydrogen evolution analysis, and electrochemical measurement. It is found that a large number of Al_2Gd, Mg_2Sn, and AlCuMg particle-like phases can be observed at the boundaries between the β-Li phase and strip-like α-Mg matrix in the as-extruded LA83-1.2Gd, LA83-1.2Sn, and LA83-1.2Cu alloys, respectively. It is also revealed that the addition of Gd and Sn can improve the corrosion resistance of extruded LA83 alloy, whereas the Cu addition decreases the corrosion resistance. This is mainly attributed to the obvious difference in potentials. Moreover, as an effective cathode, the AlCuMg phase with the miniliform shape has the highest potential difference of approximately 680 mV with respect to α-Mg matrix, which decreases the corrosion resistance. Liu et al[38] investigated the microstructure and degradation behavior of Mg-Zn-Gd-Y-Zr Mg alloys after extrusion at different temperatures and different extrusion ratios. At a given extrusion ratio, the size of dynamic recrystallized (DRXed) grains is increased with increasing the extrusion temperature. The alloys mainly consist of bimodal structures at low extrusion ratios, whereas the bimodal structure disappears when the extrusion temperature reaches 340 – 380 °C at the extrusion ratio of 12. It is reported that the alloys after extrusion at temperature of 340 °C and extrusion ratio of 12 have more DRXed fine microstructures, thereby presenting optimal corrosion resistance with corrosion rate of 0.339 mm/a. Currently, the rare earth alloying of Mg alloys mainly focuses on the mechanical properties and corrosion resistance at room temperature. However, the distribution of elements on the film layer, especially in the complex physiological conditions, is rarely reported.

Therefore, according to the current requirements of medical implanted Mg alloys, the microstructure evolution characteristics, mechanical properties, and corrosion behavior of Mg-2Zn-0.5Gd-1Y-0.5Mn Mg alloy were analyzed. This research provided the basic reference and theoretical basis for the long-term and safe service of high-performance medical Mg alloys.

1 Experiment

High purity Mg (99.94%), high-purity zinc (99.99%), and Mg-30Gd, Mg-30Y, and Mg-15Mn master alloys (wt%) were used as raw materials. The melting was conducted under Ar gas condition, which could prevent the oxidation and burning of the melting alloys. Besides, the weighed raw materials were put into the alumina crucible under vacuum states, and then they were heated to 750 °C and held for 10 min by the electromagnetic stirring until all the alloying elements were completely diffused[39]. Finally, the alloy ingot with diameter of 100 mm and the length of 100 mm was obtained by casting under argon conditions.

Before extrusion deformation, the Mg alloy ingots were homogenized at 420 °C for 24 h with specific sizes. Two magnesium alloy bars with the length of 10 mm were obtained by forward extrusion with specific extrusion ratio of 10:1 and different extrusion parameters (370 °C/0.5 $mm \cdot s^{-1}$, 390 °C/1.5 $mm \cdot s^{-1}$). The alloy composition was analyzed by the inductively coupled plasma atomic emission spectrometry, and Table 1 shows the measured composition of as-prepared Mg-2Zn-0.5Gd-1Y-0.5Mn Mg alloys.

To further explore the relationship among solute, precipitate size, and mechanical properties of as-extruded Mg alloys, the tensile deformation was conducted by the servo-hydraulic testing machine with the SANS-CMT-5105 model. Based on ASTM E8-04 standard, the measurement was performed at 25 °C with the tensile speed of 1 mm/min and specific extensometer range of 10 mm[40], as shown in Fig. 1. Additionally, the ultimate tensile strength (UTS) was calculated from the stress-strain curve. After tensile deformation, the fracture

Table 1 Measured composition of as-prepared Mg-2Zn-0.5Gd-1Y-0.5Mn Mg alloys (wt%)

Zn	Gd	Y	Mn	Mg
1.96	0.47	0.97	0.53	Bal.

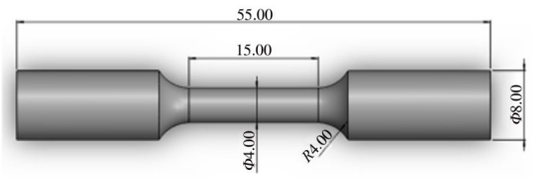

Fig.1 Schematic diagram of tensile specimens for mechanical property tests

morphologies were characterized by scanning electron microscope (SEM) coupled with energy dispersive spectrometer (EDS). The dimple sizes and the morphology of the precipitate particles were observed and analyzed. The phase components were analyzed by X-ray diffractometer (XRD).

To improve the corrosion behavior of Mg-based alloys, constant temperature static soaking and electrochemical measurements were applied. Firstly, the specimens were cut into the ones with the size of 8 mm×8 mm×8 mm, and then they were mechanically polished by SiC abrasive paper from 1000# to 2000#. Subsequently, the specimens were ultrasonically cleaned in alcohol solution and then dried in air. The specimens were weighed by electronic balance with the precision of ±0.1 mg. The test condition was as follows: Hank's solution, temperature of 37±0.5 °C, and pH value of 7.4±0.1. Afterwards, the corrosion rates were calculated based on the mass difference before and after immersion. pH value was also recorded, which was measured through the specimens with the size of 10 mm×10 mm×4 mm according to ASTM G331-12A[41].

Electrochemical tests were analyzed by the typical electrode equipment (Versa STAT 3F), which was conducted at 37±0.5 °C. Before tests, the open circuit potential was kept for 1800 s. The alternating current amplitude of the electrochemical impedance spectrum was 10 mV, and the frequency was varied from 100 kHz to 0.01 Hz. The polarization potential was varied from −0.25 V to −1.3 V, the scanning rate was 2 mV/s, and the results were fitted by Tafel software[42].

2 Results

2.1 Microstructure characteristics

SEM microstructures of Mg-2Zn-0.5Gd-1Y-0.5Mn alloys after different treatments are shown in Fig. 2. ED represents the elongation direction. As shown in Fig. 2a, the secondary phases in the as-cast alloy mainly exist in the form of long-strips and spheres. According to Fig.2b, it can be seen that the granular precipitates are distributed in the grains, and the main composition is α-Mg and W-$Mg_3Y_2Zn_3$ phases. After extrusion deformation, the precipitates break (Fig. 2c) along ED. The difference in microstructures is mainly caused by different deformation processes. Actually, the specimens extruded at 370 °C/0.5 mm·s^{-1} presents the low actual deformation temperature due to the fast dissipation in the extrusion process. Therefore, the precipitates partially break under these conditions. In addition, the complete recrystallization and dissolution of the precipitations of Mg alloys cannot be observed.

Under the extrusion condition of 390 °C/1.5 mm·s^{-1}, strong friction force occurs between the Mg ingot and extrusion machine, resulting in a large degree of deformation on Mg alloy. Besides, lots of heat is generated during the extrusion deformation process, which promotes full DRX, thereby decreasing the grain size and improving the residual stress distribution. More importantly, the amount and the volume fraction of the secondary precipitates are also decreased, compared with those after extrusion at 370 °C/0.5 mm·s^{-1}. The high temperature leads to the dissolution of more eutectic phases with low melting point in the matrix.

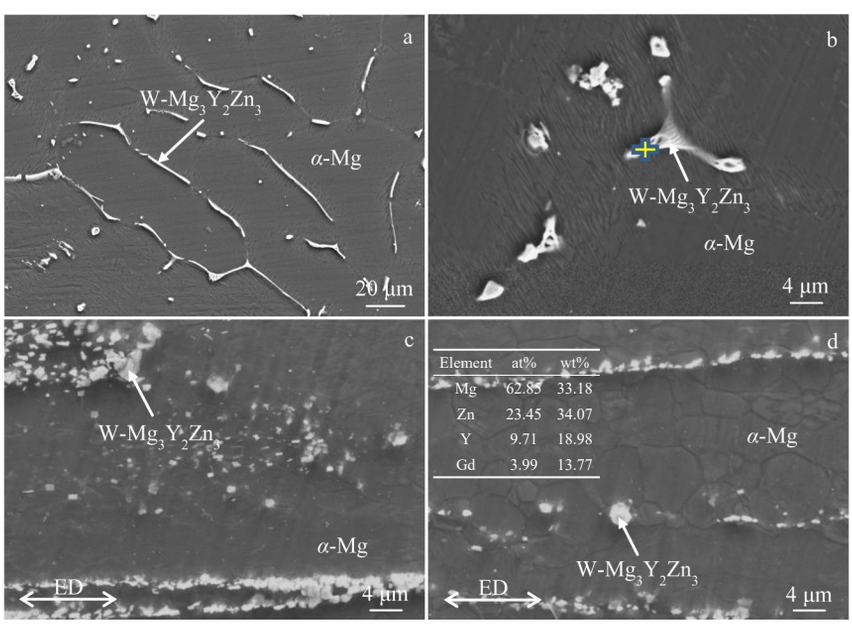

Fig.2 SEM microstructures of Mg-2Zn-0.5Gd-1Y-0.5Mn Mg alloys after different treatments: (a–b) casting; (c) extrusion at 370 °C/0.5 mm·s^{-1}; (d) extrusion at 390 °C/1.5 mm·s^{-1}

Fig. 3 shows SEM morphologies and corresponding EDS element distributions of Mg-2Zn-0.5Gd-1Y-0.5Mn Mg alloys after different treatments. Fig. 4 shows XRD patterns of Mg-2Zn-0.5Gd-1Y-0.5Mn Mg alloys after different treatments. It can be seen that the matrix of as-cast Mg alloy is mainly composed of Mg and a small amount of Zn and Mn. In addition, the distribution of Mn element in the α-Mg and W-$Mg_3Y_2Zn_3$ phases is uniform, and there is no enrichment phenomenon. According to Fig. 3b, there are more W-$Mg_3Y_2Zn_3$ phases in the Mg alloy after extrusion at 370 °C/0.5 mm·s^{-1}. However, the matrix is mainly composed of α-Mg phase. Compared with those of the as-cast Mg alloy, the specimen after extrusion at 390 °C/1.5 mm·s^{-1} has basically the same element types and phases, whereas the number of

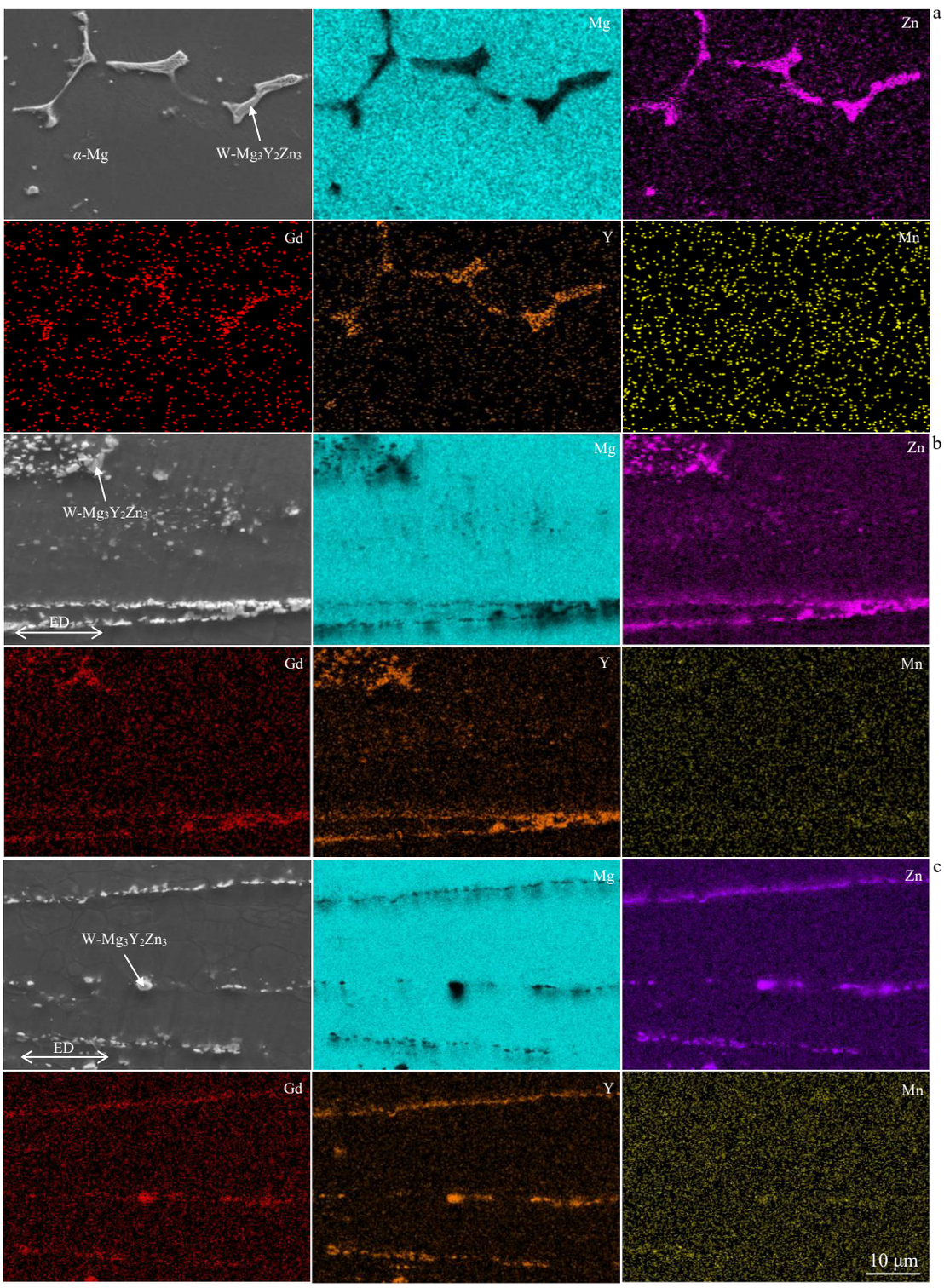

Fig.3 SEM morphologies and corresponding EDS element distributions of Mg-2Zn-0.5Gd-1Y-0.5Mn Mg alloys after different treatments: (a) casting; (b) extrusion at 370 °C/0.5 mm·s^{-1}; (c) extrusion at 390 °C/1.5 mm·s^{-1}

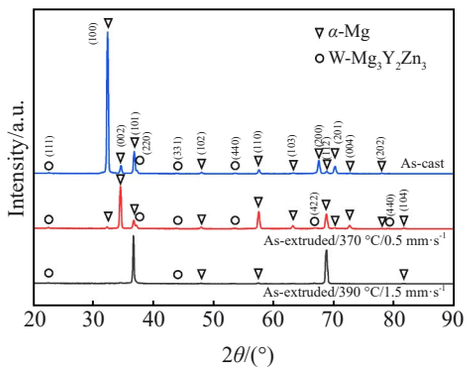

Fig.4 XRD patterns of Mg-2Zn-0.5Gd-1Y-0.5Mn Mg alloys after different treatments

secondary phases with the distribution parallel to ED is decreased.

2.2 Mechanical property measurements

In order to analyze the mechanical properties of Mg-2Zn-0.5Gd-1Y-0.5Mn Mg alloys treated by different extrusion processes, the mechanical tensile deformation at ambient temperature was conducted, and the results are shown in Fig. 5. YS stands for yield strength. The Mg-2Zn-0.5Gd-1Y-0.5Mn Mg alloy after extrusion at 370 °C/0.5 mm·s^{-1} has the highest UTS, followed by the Mg alloy after extrusion at 390 °C/1.5 mm·s^{-1}, and the as-cast Mg alloy has the lowest UTS. The Mg-2Zn-0.5Gd-1Y-0.5Mn Mg alloy after extrusion at 390 °C/1.5 mm·s^{-1} has the highest elongation, followed by the Mg alloy after extrusion at 370 °C/0.5 mm·s^{-1}, and the as-cast Mg alloy has the lowest elongation.

These results reveal that the mechanical properties of the alloys after extrusion deformation are better than those of the as-cast specimens. This improvement is related to the grain refinement effect, the increase in grain boundary density, and the fragment of the secondary precipitates after extrusion deformation[43–45], which decreases the driven force and nuclei sites of crack resources. As for the as-cast alloy, there are a large number of long-strip secondary precipitates distributed along the grain boundary regions. Due to the difference in brittleness and thermal expansibility between α-Mg phase and the secondary precipitates, the deformation step in the plastic process is inconsistent, which can easily induce the micro-cracks and accelerate the fracture of tested alloys. As for the extruded alloys, the microstructure is refined, the secondary phase is broken after deformation, and its distribution is parallel ED, which may further hinder the imitation/propagation of cracks. Thus, the comprehensive mechanical properties of the alloys can be enhanced. The specimen treated by extrusion at 370 °C/0.5 mm·s^{-1} presents the obvious work hardening behavior: high strength (258 MPa) and low ductility (13.5%), which is due to the presence of a large number of unrecrystallized grains. For the specimen treated by extrusion at 390 °C/1.5 mm·s^{-1}, the recrystallization behavior is relatively complete, and the secondary precipitates are partially dissolved into the α-Mg phase, improving the plasticity (18.5%). Besides, the strength of Mg-2Zn-0.5Gd-1Y-0.5Mn Mg alloy decreases slightly (232 MPa) due to the more uniform microstructure and the decrease in dislocation density at high temperatures.

Tensile fracture morphologies of Mg-2Zn-0.5Gd-1Y-0.5Mn Mg alloys after different treatments are shown in Fig.6. It can be seen that the as-cast specimen not only contains a lot of cleavage platforms, but also has a large number of tearing edges. In addition, a small number of dimples can be observed in Fig. 6b. Therefore, the as-cast Mg-2Zn-0.5Gd-1Y-0.5Mn Mg alloy shows the quasi-cleavage fracture features, and its inferior mechanical properties are caused by the large number of tearing edges. Although the number of dimples increases significantly in the fracture morphology of Mg-2Zn-0.5Gd-1Y-0.5Mn Mg alloy after extrusion at 370 °C/0.5 mm·s^{-1}, the tearing edges and detaching platforms still exist in the alloy, indicating that the microstructure is not sufficiently ameliorated and the grain size is not sufficiently refined. In addition, due to the existence of large-sized grains and a large number of precipitate phases, the stress concentration and fracture may easily occur during the tensile process. No tearing edge or cleavage platform can be observed in the fracture morphology for the Mg alloys extruded at 390 °C/1.5 mm·s^{-1}, inferring the ductile fracture feature. Moreover, the large number of dimples of small sizes indicates that the microstructure and grains are significantly refined during the extrusion deformation[46–49], and the precipitate distribution becomes more

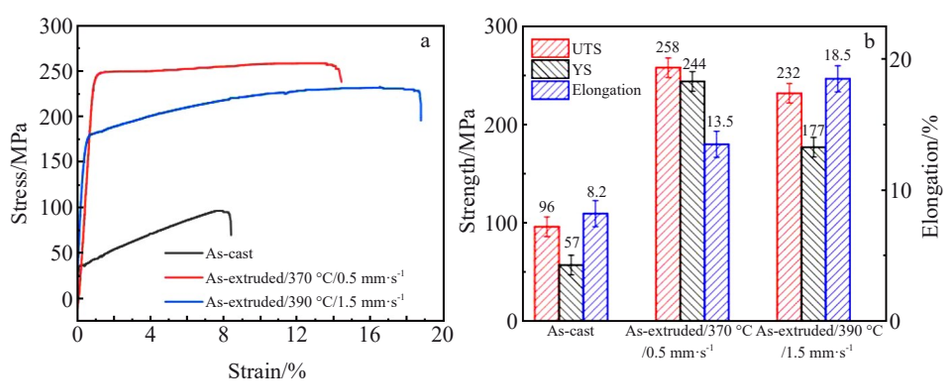

Fig.5 Stress-strain curves (a) and mechanical properties (b) of Mg-2Zn-0.5Gd-1Y-0.5Mn Mg alloys after different treatments

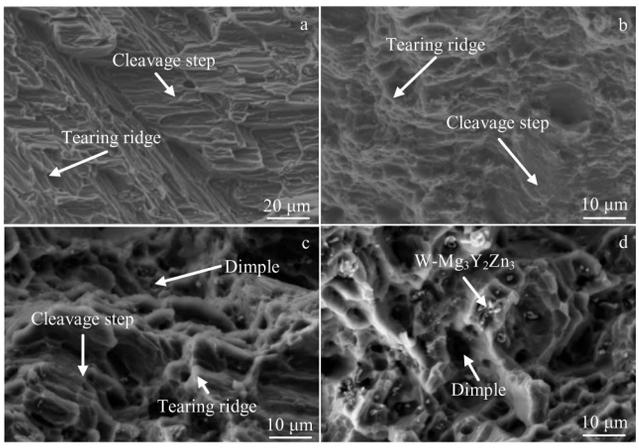

Fig.6 Tensile fracture morphologies of Mg-2Zn-0.5Gd-1Y-0.5Mn Mg alloys after different treatments: (a–b) as-cast; (c) extrusion at 370 °C/0.5 mm·s^{-1}; (d) extrusion at 390 °C/1.5 mm·s^{-1}

uniform/dispersed. Thus, the alloy elongation is improved.

2.3 Immersion and electrochemical test

In order to simulate the corrosion performance of alloy implants in complicated physiological environment, some accelerated simulation experiments were conducted, such as static immersion, pH, hydrogen evolution, and electrochemical tests[50–52]. Fig. 7 shows the hydrogen evolution rates and average corrosion rates of Mg-2Zn-0.5Gd-1Y-0.5Mn Mg alloys after different treatments. It can be seen that the hydrogen evolution of as-cast and extruded Mg alloys is increased with prolonging the soaking time (Fig.7a). When the soaking time reaches 30 d, the hydrogen evolution capacity is 5.52, 7.75 and 4.43 mL·cm^{-2} for the Mg-2Zn-0.5Gd-1Y-0.5Mn Mg alloys after cast treatment, extrusion at 370 °C/0.5 mm·s^{-1}, and extrusion at 390 °C/1.5 mm·s^{-1}, respectively. Normally, the hydrogen evolution rate and corrosion rate can both directly reflect the corrosion degree. However, in this research, the corrosion degree obtained by measured corrosion rate of as-cast and extruded Mg alloys is obviously higher than that obtained by hydrogen evolution rate. It is because some hydrogen may dissolve into the Hank's simulated body fluid (SBF) during the hydrogen evolution. In addition, when the specimen is rinsed/cleaned, the matrix is corroded to a certain extent, which further aggravates the corrosion degree. The variation of pH value of Mg-2Zn-0.5Gd-1Y-0.5Mn Mg alloys in Hank's solution for 20 d is shown in Fig.7c. It can be seen that the pH value of the as-cast and as-extruded Mg alloys is increased with prolonging the soaking time.

The polarization results of the Mg-2Zn-0.5Gd-1Y-0.5Mn alloys in Hank's electrolyte solution are shown in Fig. 7d. It can be seen that the anode branches of all alloys present the obvious inflection points due to the formation of dense protective layer on the alloy surface in SBF, which can further hinder the corrosion dissolution. Besides, for the Mg-2Zn-0.5Gd-1Y-0.5Mn alloys after casting, extrusion at 370 °C/0.5 mm·s^{-1}, and extrusion at 390 °C/1.5 mm·s^{-1}, the self-corrosion potentials are −1.536, −1.554, and −1.521 V, and the corrosion current densities are 2.498, 3.656, and 1.012 μA·cm^{-2}, respectively. According to the relationship between current

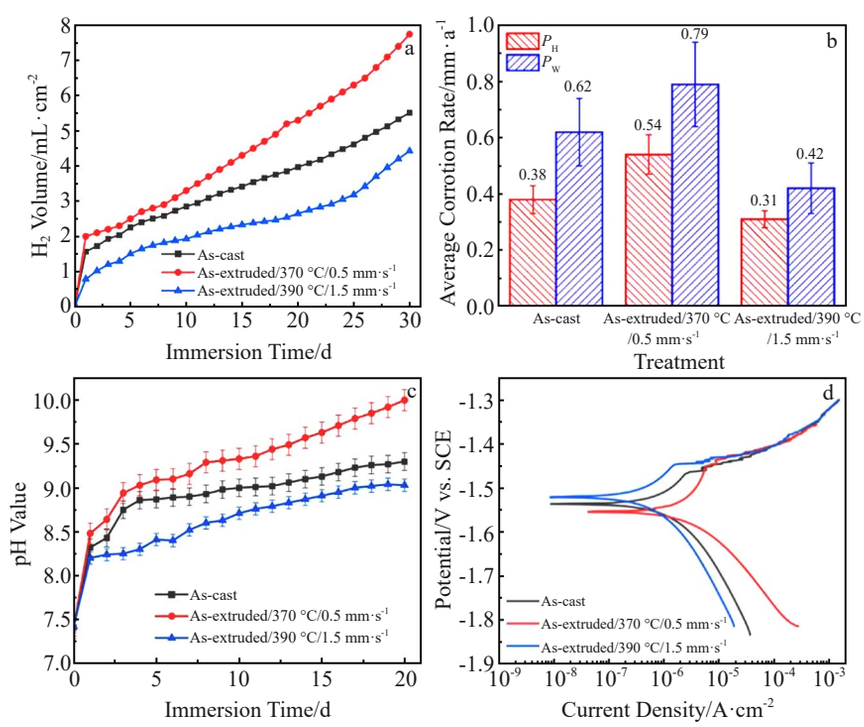

Fig.7 Hydrogen evolution rates (a), average corrosion rates (b), pH values (c), and polarization curves (d) of Mg-2Zn-0.5Gd-1Y-0.5Mn Mg alloys after different treatments immersed in Hank's solution (P_H indicates the corrosion rate obtained by hydrogen release volume; P_W indicates the corrosion rate obtained by mass loss)

density and corrosion resistance, the results further reveal that the Mg alloy extruded at 370 °C/0.5 mm·s^{-1} presents the worst corrosion resistance, and the Mg alloy extruded at 390 °C/1.5 mm·s^{-1} possesses the optimal corrosion resistance. This is because during extrusion at 370 °C/0.5 mm·s^{-1}, the secondary precipitates of Mg alloys are partially broken. But they are not dissolved into the matrix due to the relatively low temperature. Thus, the density of the secondary precipitates increases and the contact area ratio is enlarged. As a result, the corrosion resistance of the Mg alloys extruded at 370 °C/0.5 mm·s^{-1} is inferior, even compared with that of the as-cast specimen.

In order to analyze the corrosion mechanism of rare earth alloying on Mg alloys in SBF, the Mg-2Zn-0.5Gd-1Y-0.5Mn alloys after casting treatment and extrusion at 390 °C/1.5 mm·s^{-1} were selected for comparison. The Mg-2Zn-0.5Gd-1Y-0.5Mn alloy after extrusion at 390 °C/1.5 mm·s^{-1} is called as the as-extruded Mg alloy for short in the following discussion. SEM morphologies of different alloy surfaces before and after corrosion product removal are shown in Fig.8 and Fig.9, respectively. Initially, a large number of $Mg(OH)_2$ products are formed on both the as-cast and as-extruded Mg alloys after immersion for 10 d. However, the loose porous magnesium hydroxide layer in Cl^--rich simulated fluid environment can easily form micro-cracks, affecting the corrosion resistance. In addition, due to the increase in local pH, a certain amount of phosphate is deposited on the hydroxide/oxide surface, which is beneficial to enhance the corrosion resistance. However, after immersion for 20 d, a large amount of Cl^- in the solution is consumed, resulting in the increase in pH value of the solution and a significant increase in the phosphate precipitates. Additionally, the $Mg(OH)_2$ film layer on the Mg alloy surface is thickened due to the direct contact between the large amount of OH^- and the Mg alloy matrix, especially in the surface of as-cast specimen (local-upwarp). After immersion for 30 d, the surface of Mg alloys is covered by the phosphate precipitation. The mineralization process reduces the contact area between SBF and fresh Mg matrix, resulting in slower corrosion rate and stable pH value of the solution.

After corrosion product removal, a few large-scale corrosion pits appear on the surface of the as-cast Mg alloy, presenting the shallow and flat morphology. After immersion for 20 and 30 d, the corrosion area and size of the alloys are enlarged and the as-cast alloy presents the uneven morphology. Conversely, the corrosion rate of as-extruded magnesium alloy is obviously slow, and only a few small corrosion pits appear on the surface after immersion for 10 d. However, after immersion for 20 d, the number and the depth of small pits on the alloy surface are increased, but the corrosion area on the surface changes slightly. After immersion for 30 d, some small pits are in contact with each other and a few large-sized pits appear. In conclusion, the as-extruded Mg-2Zn-0.5Gd-1Y-0.5Mn Mg alloy has better corrosion resistance than the as-cast Mg alloy does.

3 Discussion

The corrosion rates of Mg-based alloys not only are related to the material properties, but also correspond to the environment conditions[53–55]. In order to accurately measure the corrosion rate of as-cast and as-extruded Mg alloys, Hank's SBF was used in all experiments. Due to various elements in Hank's SBF, the corrosion process of Mg alloys is accompanied by the dissolution and produces various degradation products on the surface, which has a certain impact on the corrosion process[56–58]. According to Fig. 2 and Fig. 4, the composition of Mg-2Zn-0.5Gd-1Y-0.5Mn Mg alloys is mainly the α-Mg phase with a little W-$Mg_3Y_2Zn_3$ precipitate phase. Due to the potential difference between α-Mg and W-

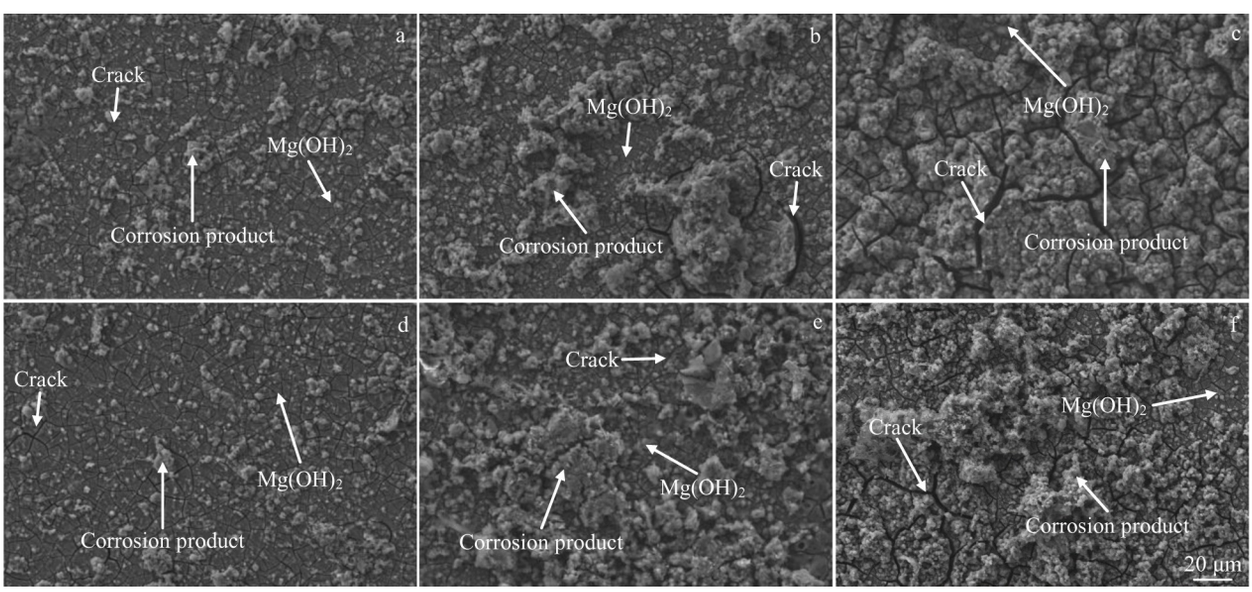

Fig.8 SEM surface morphologies of as-cast (a–c) and as-extruded (d–f) Mg-2Zn-0.5Gd-1Y-0.5Mn Mg alloys immersed in Hank's solution for 10 d (a, d), 20 d (b, e), and 30 d (c, f) before corrosion product removal

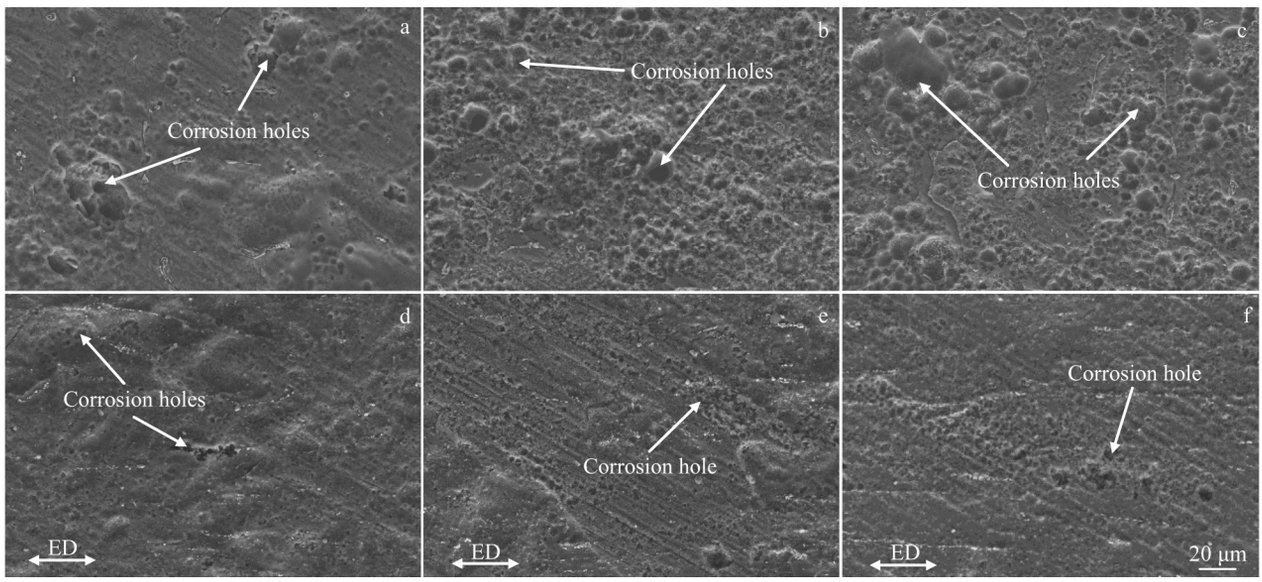

Fig.9 SEM surface morphologies of as-cast (a–c) and as-extruded (d–f) Mg-2Zn-0.5Gd-1Y-0.5Mn Mg alloys immersed in Hank's solution for 10 d (a, d), 20 d (b, e), and 30 d (c, f) after corrosion product removal

$Mg_3Y_2Zn_3$ phases, the corrosion galvanic couples can be easily formed in the solution environment, where the matrix is the anode and the secondary phase is the cathode, accelerating the dissolution of the alloy matrix. The reactions are as follows:

$$Mg \rightarrow Mg^{2+} + 2e^- \quad (1)$$

$$2H_2O + 2e^- \rightarrow 2OH^- + H_2 \uparrow \quad (2)$$

$$Mg + 2H_2O \rightarrow Mg(OH)_2 \downarrow + H_2 \uparrow \quad (3)$$

It can be seen that the magnesium hydrate degradation layer can be instantaneously formed under the corrosion medium condition. Due to the porous multi-defect features, the protect effect is weak. With increasing the OH^- content and pH value, the deposition of phosphates and other substances on the surface is accelerated. Due to its stability and compactness, the deposited product is beneficial to improve the corrosion resistance of the Mg matrix. Besides, the improvement in corrosion resistance is very limited due to the small content of deposited product.

The erosive Cl^- can directly penetrate the product layer of magnesium hydroxide, contact with the magnesium alloy matrix, and accelerate the reaction. Cl^- also reacts with $Mg(OH)_2$ to form $MgCl_2$, resulting in corrosion and damage of $Mg(OH)_2$ film. The detailed process can be listed as follows:

$$Mg + 2H^+ \rightarrow Mg^{2+} + H_2 \quad (4)$$

$$Mg(OH)_2 + 2H^+ \rightarrow Mg^{2+} + 2H_2O \quad (5)$$

$$Mg(OH)_2 + 2Cl^- \rightarrow MgCl_2 + 2OH^- \quad (6)$$

It can be seen that the results of hydrogen evolution are consistent with the results of pH value, electrochemical test, and immersion test. With the corrosion reaction proceeding, the adjacent small corrosion pits are in contact with each other and merge into the large-sized pits, and a large number of hydroxide ions are generated. Besides, Ca^{2+} in SBF environment can be mineralized with PO_4^{3-}, HPO_4^{2-}, and OH^-, forming a certain amount of phosphate deposit on the surface, which hinders the corrosion process. The schematic diagrams of as-cast and as-extruded Mg-2Zn-0.5Gd-1Y-0.5Mn Mg alloys in SBF environment are shown in Fig.10.

As shown in Fig. 2, the extrusion deformation can change the precipitate distribution in Mg alloys. In the extrusion deformation, the large strip precipitate phase in the as-cast Mg alloys are broken into short bars and distributed in the grains, resulting in the size reduction of the secondary phases. Normally, W phase in Hank's SBF can easily form micro-galvanic corrosion with α-Mg phase, which accelerates the corrosion of magnesium alloys. However, the W phase is broken after extrusion deformation and partially dissolved into the matrix, resulting in a decrease in the cathode area. Thus, the corrosion dissolution rate of the Mg alloys is further reduced due to the decrease in micro-galvanic corrosion driving force. Additionally, the microstructure is refined after extrusion deformation and the density of grain boundaries is increased because of DRX, which also enhances the corrosion

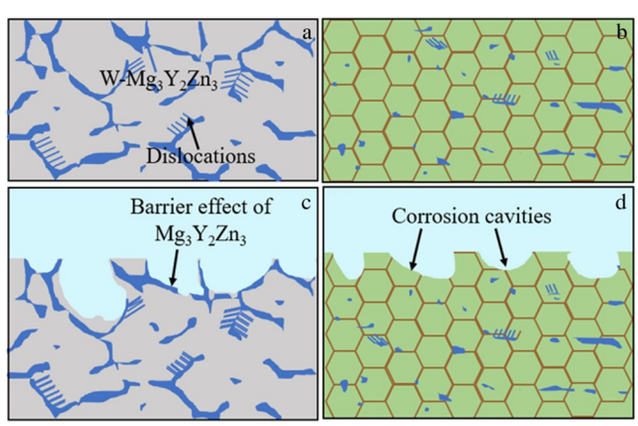

Fig.10 Schematic diagrams of as-cast (a–b) and as-extruded (c–d) Mg-2Zn-0.5Gd-1Y-0.5Mn Mg alloys in SBF environment

resistance and changes the pitting corrosion model into uniform corrosion.

According to the abovementioned microstructure characterization and reaction process, the specific reaction process can be divided into three steps. (1) When the magnesium matrix is in contact with the Cl-rich corrosion solution, the bubble aggregation phenomenon occurs rapidly, which is accompanied by the precipitation of a large number of white Mg hydroxides. Due to the presence of a large amount of Cl^-, $MgCl_2$ is continuously formed. Meanwhile, the calcium and magnesium ions in the solution continuously undergo the deposition reactions with hydrogen phosphate ions, phosphate ions, and hydroxide ions. (2) With the corrosion reaction proceeding, some insoluble salts begin to appear/deposit on the alloy surface, such as phosphate and carbonate. Due to the surface stress and low Pilling-Bedworth ratio (Pilling-Bedworth ratio of less than 1 indicates the loose porosity), the formed degradation layer is not compact and complete, which promotes the partial dissolution in the solution. Additionally, the micro-cracks/micro-voids within the degradation layer provide a convenient channel for the highly erosive chloride ions with small radius to move to the front side of interface. The dissolved magnesium ions can also migrate to the alloy surface through the loose corrosion products. (3) Ion precipitation and product deposition occur continuously under the driven force of reaction chemical potentials, resulting in more and more corrosion products. Besides, the thickness of degradation layer increases, and the defects of degradation layer are more and more diverse. With the corrosion reaction proceeding, the corrosion rupture area of alloys is expanded and the surface products gradually collapse and are folded. Besides, the corrosion micro-pores at the bottom of product layer also begin to gather and develop horizontally and longitudinally until they interpenetrate and interact with each other.

4 Conclusions

1) The microstructures of as-cast and as-extruded Mg-2Zn-0.5Gd-1Y-0.5Mn Mg alloys at room temperature are mainly composed of α-Mg and W phases. This result is caused by the complete dynamic recrystallization process. The extrusion deformation does not change the precipitate type, but changes its distribution and morphology.

2) Compared with those of the as-cast Mg-2Zn-0.5Gd-1Y-0.5Mn Mg alloy, the mechanical properties of the as-extruded (370 °C/0.5 $mm \cdot s^{-1}$) alloys are significantly improved: the ultimate tensile strength is 232 MPa and elongation is 18.5%. On the one hand, the extrusion deformation eliminates the defects, such as loose holes, and breaks the large-scale precipitates, thus reducing the crack initiation source. On the other hand, the dynamic recrystallization of magnesium alloys easily occurs during the hot deformation, which is beneficial to optimize the mechanical properties.

3) Compared with that of the as-cast Mg-2Zn-0.5Gd-1Y-0.5Mn Mg alloy, the corrosion resistance of the as-extruded (390 °C/1.5 $mm \cdot s^{-1}$) alloys is enhanced: the optimal current density of 1.012 $\mu A/cm^2$. On the one hand, the large proportion of fine-crystal structure (high-density active atoms) is beneficial to provide nuclei particles for the formation of film layer when it comes into contact with the corrosion solution. On the other hand, the adhesion and integrity between the film layer and the matrix are improved, thus reducing the hydrogen evolution rate and improving the corrosion resistance.

References

1 Zerankeshi M M, Alizadeh R. *Materialia*[J], 2022, 23: 101 445
2 Xing F, Li S, Yin D D *et al*. *Journal of Magnesium and Alloys*[J], 2022, 10(6): 1428
3 Liu Y, Zhang Y, Wang Y L *et al*. *Journal of Alloys and Compounds*[J], 2021, 885: 161 001
4 Tsakiris V, Tardei C, Clicinschi F M. *Journal of Magnesium and Alloys*[J], 2021, 9(6): 1884
5 Tong P D, Sheng Y L, Hou R Q *et al*. *Smart Materials in Medicine*[J], 2022, 3: 104
6 He H, Li K, Luo W *et al*. *Surface and Coatings Technology*[J], 2022, 443: 128 643
7 Zhang Yuan, Zheng Ruining, Liu Yun *et al*. *Rare Metal Materials and Engineering*[J], 2023, 52(1): 374 (in Chinese)
8 Zhang B X, Zhang W, Zhang F *et al*. *Journal of Magnesium and Alloys*[J], 2022
9 Wang D W, Dong K J, Jin Z Z *et al*. *Journal of Alloys and Compounds*[J], 2022, 914: 165 325
10 Sun J, Du W B, Fu J J *et al*. *Journal of Magnesium and Alloys*[J], 2022, 10(10): 2649
11 Dong J H, Lin T, Shao H P *et al*. *Journal of Alloys and Compounds*[J], 2022, 908: 164 600
12 Liu L, Yu S R, Liu E Y *et al*. *Materials Chemistry and Physics*[J], 2021, 271: 124 935
13 Xu Y Z, Li J Y, Qi M F *et al*. *Materials Characterization*[J], 2022, 188: 111 867
14 Zhou W H, Yan J L, Li Y Y *et al*. *Biomaterials Science*[J], 2021, 9(3): 807
15 Li M, Huang Y C, Liu Y *et al*. *Materials Science and Engineering A*[J], 2022, 832: 142 479
16 Su N, Wu Y J, Deng Q C *et al*. *Materials Science and Engineering A*[J], 2021, 810: 141 019
17 Wu P F, Lou Y S, Chen Q *et al*. *International Journal of Mechanical Sciences*[J], 2022, 229: 107 506
18 Lei B, Dong Z H, Yang Y *et al*. *Materials Science and Engineering A*[J], 2022, 843: 143 136
19 Zhu Q C, Li Y X, Ding Z G *et al*. *Materials & Design*[J], 2021, 202: 109 570
20 Ma Y J, Liu C M, Jiang S N *et al*. *Materials Letters*[J], 2022, 320: 132 363
21 Xiang H L, Zeng W J, Lang Y X *et al*. *Journal of Alloys and Compounds*[J], 2023, 945: 169 312
22 Chen Y W, Li Q, Li Y X *et al*. *Journal of Materials Science & Technology*[J], 2022, 126: 80
23 Yin S Q, Duan W C, Liu W H *et al*. *Corrosion Science*[J], 2020, 177: 108 962
24 Wang S D, Xu D K, Wang B J *et al*. *Corrosion Science*[J], 2018, 142: 185

25 Dai J W, Dong Q S, Nie Y J *et al*. *Materials & Design*[J], 2022, 221: 110 980
26 Luo Y F, Deng Y L, Guan L Q *et al*. *Corrosion Science*[J], 2020, 164: 108 338
27 Wang X J, Chen Z N, Guo E Y *et al*. *Journal of Alloys and Compounds*[J], 2021, 863: 158 762
28 Sun L X, Dong N N, Wang J H *et al*. *Corrosion Science*[J], 2022, 196: 110 023
29 Lei L, Cui Z Y, Pan H *et al*. *Corrosion Science*[J], 2022, 195: 109 975
30 Xie J S, Zhang J H, Zhang Z *et al*. *Journal of Materials Research and Technology*[J], 2022, 19: 30
31 He D L, Gong H, Zhang Z Y *et al*. *Corrosion Science*[J], 2022, 208: 110 621
32 Peng X, Sun J W, Liu H J *et al*. *Transactions of Nonferrous Metals Society of China*[J], 2022, 32(1): 134
33 Gerashi E, Alizadeh R, Langdon T G. *Journal of Magnesium and Alloys*[J], 2022, 10(2): 313
34 Hsieh C Y, Huang S Y, Chu Y R *et al*. *Journal of Materials Research and Technology*[J], 2023, 22: 2343
35 Xin L N, Zhou J Q, Mei D *et al*. *Journal of Alloys and Compounds*[J], 2023, 934: 168 044
36 Li L H, Bao J X, Qiao M L *et al*. *Materials Science and Engineering A*[J], 2023, 872: 144 979
37 Hu Z, Yin Z, Yin Z *et al*. *Corrosion Science*[J], 2020, 176: 108 923
38 Liu Y, Wen J B, Li H *et al*. *Journal of Alloys and Compounds*[J], 2022, 891: 161 964
39 Zhang Y, Li J Y, Liu Y *et al*. *Materials Characterization*[J], 2020, 165: 110 368
40 American Society for Testing and Materials. ASTM E8-04[S], 2004
41 American Society for Testing and Materials. ASTM G331-12A[S], 2004
42 Zhao J, Jiang B, Xu J *et al*. *Materials Science and Engineering A*[J], 2022, 839: 142 867
43 Zhu Q C, Shang X Q, Zhang H *et al*. *Materials Science and Engineering A*[J], 2022, 831: 142 166
44 Lei B, Dong Z H, Yang Y *et al*. *Materials Science and Engineering A*[J], 2022, 843: 143 136
45 Peng P, She J, Tang A T *et al*. *Journal of Alloys and Compounds*[J], 2022, 890: 161 789
46 Lv H, Li L, Wen Z Z *et al*. *Materials Science and Engineering A*[J], 2022, 833: 142 521
47 Emamy M, Mirzadeh H, Raayatpour M *et al*. *Materials Science and Engineering A*[J], 2022, 840: 142 996
48 Yan L, Zhang Z M, Xue Y *et al*. *Journal of Alloys and Compounds*[J], 2022, 906: 164 406
49 Hou C H, Cao H S, Qi F G *et al*. *Journal of Magnesium and Alloys*[J], 2022, 10(4): 993
50 Mardina Z, Venezuela J, Dargusch M S *et al*. *Corrosion Science*[J], 2022, 199: 110 160
51 Zohdy K M, El-Sherif R M, El-Shamy A M. *Chemical Papers*[J], 2023, 77: 1317
52 Zhang Y, Cao J, Wang X L *et al*. *Bioactive Materials*[J], 2022, 7: 217
53 Tsakiris V, Tardei C, Clicinschi F M. *Journal of Magnesium and Alloys*[J], 2021, 9(6): 1884
54 Li H F, Huang Y, Ji X J *et al*. *Journal of Materials Science & Technology*[J], 2022, 131: 48
55 Wang J, Dou J H, Wang Z C *et al*. *Journal of Alloys and Compounds*[J], 2022, 923: 166 377
56 Xie J S, Zhang J H, Zhang Z *et al*. *Corrosion Science*[J], 2022, 198: 110 163
57 Wang D, Dong K, Jin Z *et al*. *Journal of Alloys and Compounds* [J], 2022, 914: 165 325
58 Kousis C, Keil P, McMurray H N *et al*. *Corrosion Science*[J], 2022, 206: 110 477

挤压态Mg-2Zn-0.5Gd-1Y-0.5Mn合金的组织特征、力学性能和体外腐蚀行为

赫荣辉[1]，王　晗[2]，张　泽[3,4]，李静媛[2]，文良元[3,4]

(1. 中国核工业集团有限公司 中国核动力研究设计院，四川 成都 610213)

(2. 北京科技大学 材料科学与工程学院，北京 100083)

(3. 北京医院 骨科，北京 100730)

(4. 中国医学科学院 国家老年医学中心，北京 100730)

摘　要：为改善医用镁合金微观组织特征与降解行为，采用挤压形变工艺改变医用镁合金的晶粒尺寸特征及析出相/金属间化合物尺寸、分布规律，探究了挤压态医用Mg-2Zn-0.5Gd-1Y-0.5Mn镁合金微观结构特征及降解行为。结果表明：不同的热挤压变形并没有改变Mg-2Zn-0.5Gd-1Y-0.5Mn镁合金中第二相的类型，但改变了第二相的分布和形貌。Mg-2Zn-0.5Gd-1Y-0.5Mn镁合金的成分主为α-Mg和W-$Mg_3Y_2Zn_3$。电化学测试结果表明，铸态、挤压370 ℃和挤压390 ℃合金腐蚀电流密度分别为2.498、3.656、1.012 μA·cm^{-2}。这是由于铸态组织中析出相/金属间化合物呈带状分布在基体中，可作为微阴极形成电偶腐蚀位点，加速合金腐蚀速率。合金在370 ℃挤压时，由于实际温度较低，部分粗化相未能充分溶解到α-Mg基体中，随着析出相数量增加及分布混乱无序，微阴极面积比例增大，进而导致腐蚀速率加剧。而390 ℃挤压态镁合金的挤压速度快、耗散行为慢，且铸锭与挤压机间摩擦强烈，已发生充分动态再结晶行为，降低了微阴极数量/面积，增强了合金耐腐蚀性能。

关键词：挤压温度；显微组织；析出相；腐蚀行为；可降解镁合金

作者简介：赫荣辉，男，1979年生，硕士，高级工程师，中国核工业集团有限公司中国核动力研究设计院，四川 成都 610213，E-mail：heronghui007@163.com